Plasmonics (2023) 18:1581–1591
https://doi.org/10.1007/s11468-023-01881-2

RESEARCH

Near- and Mid- Infrared Quintuple-Band Plasmonic Metamaterial Absorber

Chung-Ting Chou Chao[1] · Sy-Hann Chen[2] · Hung Ji Huang[3] · Yuan-Fong Chou Chau[4]

Received: 25 April 2023 / Accepted: 11 May 2023 / Published online: 18 May 2023

Abstract

In nanophotonic devices, the absorption of electromagnetic waves plays a critical role. Attempting to achieve narrowband absorption with multiple operating wavelengths, particularly in the near- and mid-infrared regions, is still a challenging endeavor. In this study, we developed a plasmonic metamaterial absorber (PMA) with a quintuple-band design. This PMA uses a periodic structure consisting of a dielectric layer sandwiched between a metallic nanobar array and a thin Ag film. The PMA can operate in both the near-infrared and mid-infrared regions. The absorptance of the proposed PMA for modes 1–5 is 98.02%, 99.47% 98.02%, 99.47%, and 96.09%, respectively. The high absorptance is due to hybridization of localized gap, cavity and surface plasmon resonance. This phenomenon can be explained by an inductance and capacitance circuit model. We also investigated the effects of structure parameters on the absorptance spectrum, which will provide valuable guidance for designing high-performance PMA.

Keywords Plasmonic absorber · Finite element method · Sensitivity · Biosensor

Introduction

Surface plasmon polaritons (SPPs) refer to electromagnetic (EM) waves that are confined and transmitted at the boundary between a metal and a dielectric material [1–5]. SPPs can be controlled using waveguides and resonators and have the potential to be useful in a variety of nanophotonic applications such as optical sensing, optical communication, photonic energy harvesting, and the development of integrated optical circuits (IOCs), due to their ability to concentrate and direct EM energy at the nanoscale [6–8]. In recent years, metamaterials have gained significant attention for their unique optical properties and have been successfully incorporated into a variety of meta-devices for use in different areas of nanophotonics [9–12].

Plasmonic metamaterial absorbers (PMAs), which are a type of metamaterial, have shown remarkable abilities to manipulate electromagnetic waves, which typically consist of periodic sub-wavelength metallic and dielectric units [13, 14]. These PMAs are designed to efficiently harvest EM radiation through an impedance-matching mechanism [15]. Compared to traditional absorbers, PMAs offer several advantages, such as greater miniaturization, improved adaptability, and increased effectiveness [16, 17]. Furthermore, PMAs have potential for use in a diverse range of applications, such as emitters, sensors, modulators, infrared camouflage, optical communication, and more [18–21].

PMAs are designed with a specific structural design that enables them to absorb light from a particular wavelength range with high efficiency [19]. In the microwave region (wavelengths of several millimeters to a few centimeters), PMAs can be designed using periodic arrays of metallic structures, such as split-ring resonators, to achieve strong absorption [22]. In the optical wavelength range (typically in the range of hundreds of nanometers), PMAs can be designed using structures such as nanowires, nanorods, and nanodisks [23]. The mid-infrared range is highly suitable

✉ Yuan-Fong Chou Chau
chou.fong@ubd.edu.bn

1 Department of Optoelectronics and Materials Technology, National Taiwan Ocean University, Keelung 20224, Taiwan

2 Department of Electrophysics, National Chiayi University, Chiayi 600, Taiwan

3 Department of Electra-Optical Engineering, National Formosa University, No.64, Yunlin County 632, Huwei, Taiwan

4 Centre for Advanced Material and Energy Sciences, Universiti Brunei Darussalam, Tungku Link, Gadong BE1410, Brunei Darussalam

for biosensing because it includes molecular vibrations that uniquely characterize the biochemical components of living organisms [24]. In the mid-infrared wavelength range (typically between 2 and 20 μm), various strategies have been developed to design PMAs, including composite grating superabsorbers, photonic crystal superabsorbers, and broadband nanoresonator absorbers [25]. These strategies involve designing complex structures that can efficiently trap and absorb light of different wavelengths in this range. The improved sensitivity of PMAs in chemical and biological sensing applications is due to their ability to absorb light in a specific wavelength range and interact with the surrounding environment in a controlled way. This makes PMAs useful in a wide range of sensing applications, including environmental monitoring, medical diagnostics, and food quality control [26, 27].

Based on this assumption, achieving perfect dual or multiband absorption requires a compound unit cell compound or a multilayered structure, making the manufacturing process more complex [15]. Consequently, there is a need to design a relatively simple structure that exhibits dual or multiband perfect absorption while being insensitive to polarization. This feature has been less demonstrated in previous research studies and is highly desirable.

Numerous research groups have utilized various techniques to enhance the performance by manipulating the parameters of materials and geometries, as well as by hybridizing plasmonic and electromagnetic wave coupling. Porous and tubular metal nanostructure arrays have garnered significant attention in the development of biosensors [28, 29]. These structures possess an open surface morphology and provide a conducive environment for label-free biosensing on metal nanoparticle surfaces, thereby offering multiple advantages. Han et al. developed a plasmonic absorber by decorating a hexagonal array of silicon nanowires (SiNW) with Au nanoparticles, achieving a broadband absorption of more than 80% in the range of 400 to 1000 nm [30]. The wideband absorption was due to cavity modes in the SiNWs and surface plasmon polaritons on the AuNPs. Liu et al. created an ultra-narrow band perfect absorber using a periodic structure, which operated in the near-infrared region [31]. Cao et al. proposed a perfect plasmonic absorber (PMA) consisting of a metal substrate and a periodic array of silicon nanorod resonators (SNRRs) for visible light, achieving an absorbance exceeding 92.2% [32]. Cheng et al. designed a triple narrowband PMA with vertical square split ring (VSSR) resonators with polarization-insensitive vertical polarization, achieving a maximum absorptance of 99.80% [33]. Luo et al. numerically investigated a perfect narrow-band absorber based on a metal–metal-dielectric-metal structure that consists of periodic metallic nanoribbon arrays. Their absorber presents a nearly perfect absorption of more than 99.9% in the infrared region [34]. Note that single-band PMAs are not suitable in some areas, such as spectroscopic detection and phase imaging, which require distinct absorption bands [35]. Therefore, research on more advanced multiband perfect MAs is necessary, and now has become a hot area.

A PMA can induce electric and magnetic resonances simultaneously to ensure impedance matching with the

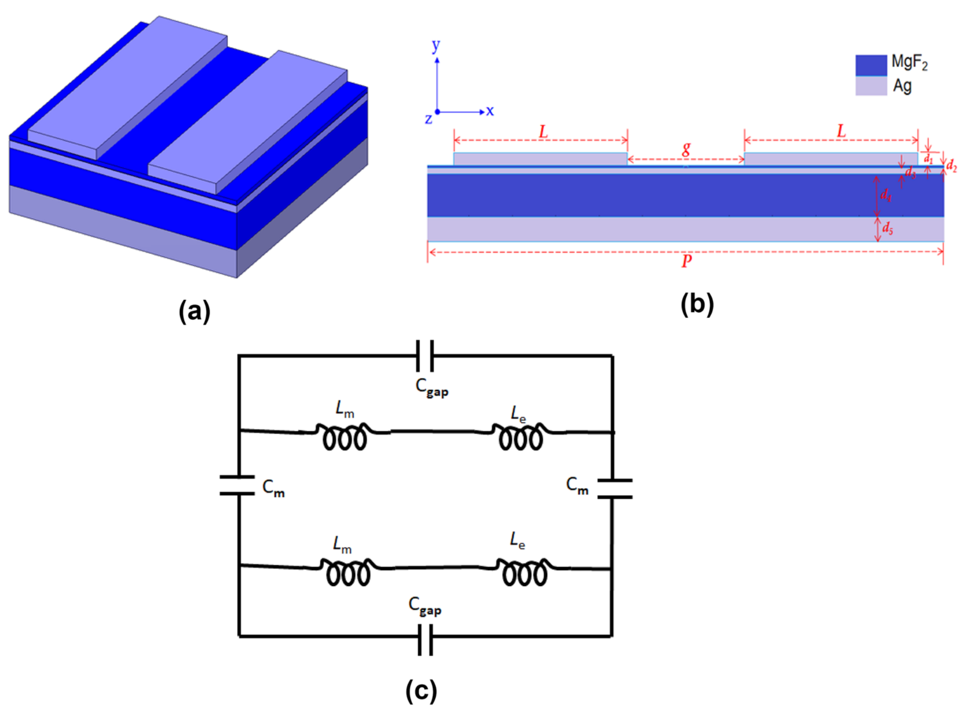

Fig. 1 Unit cells and geometrical parameters of the proposed PMA structures, (**a**) 3D view and (**b**) the cross section of the 2D view and the design parameters of the structure. (**c**) Schematic of the equivalent *LC* circuit for the proposed PM structure

Table 1 The corresponding parameters of the LC circuit model

symbol	definition	expression
L_m	the mutual inductance of the Ag nanobars and Ag layers	$L_m = 0.5\ \mu_0 L d_2$
μ_0	the permeability of surrounding environment	$\mu_0 = 1.00$ (in air)
ε_0	the dielectric permittivity of the surrounding environment	$\varepsilon_0 = 1.00$ (in air)
L_e	the kinetic inductance	$L_e = L/\ \gamma\varepsilon_0 d_1 \omega^2_p$
γ	a factor considering the effective cross-sectional area of the Ag nanobars	
ω_p	the plasma frequency of the Ag	
C_{gap}	The capacitance between the two Ag nanobars	$C_g = \pi\varepsilon_0/(g/d_1)$
C_m	the parallel plate capacitor C_m between the upper Ag nanobars and the Ag layer	$C_m = c_1\varepsilon_2\varepsilon_0 L/d_2$
c_1	a numerical factor accounting for the non-uniform charge distribution at the Ag surfaces	
ε_2	the dielectric permittivity of the dielectric spacer (i.e., MgF_2)	

surrounding medium. This leads to nonreflection at the incident interface. There are two main types of PMAs: narrowband and broadband [36, 37]. Metamaterial absorbers are a viable option to enhance the performance of photodetectors. However, achieving narrowband absorption with multiple working wavelengths, particularly in the near and mid-infrared regions, is still a challenging endeavor. This study was motivated by previous articles and focused on the important topic of light-matter interaction at the PMA interface. The aim of the study was to design a quintuple narrowband plasmonic perfect absorber with a periodic structure that could function as an ultrasensitive RI sensor in the visible, near-infrared, and mid-infrared regions. The absorber was created using a dielectric layer sandwiched between a metallic nanobar array and a thin Ag film, supported by an assembly of six alternative Si-Ag films. The absorbance was over 90% at five different resonance frequencies under normal incidence. The perfect absorption was analyzed through electric- and magnetic-field distributions using COMSOL Multiphysics, and the working band and range of the absorptance peaks could be actively tuned by changing material parameters. The absorptance peak also showed high sensitivity to the variation of RI in the ambient medium. The designed sensor based on the perfect plasmonic absorber had a high sensitivity of around 98.02%, 99.47%, 98.02%, 99.47%, and 96.09% for modes 1–5, respectively. Thus, the quintuple narrowband perfect absorber has the potential for use in enhanced sensing and spectroscopy applications.

Simulation Models and Fundamental

In the near-infrared or mid-infrared region, PMAs usually consist of a trilayer structure [38]. In Fig. 1(a), the 3D view of the unit cell for the five-band PMA configuration. The PMA system within the unit cell exhibits a hybridization of the surface plasmon resonance (SPR) and cavity plasmon resonance (CPR) nanostructure, which comprises a periodic array of a pair of Ag nanobars adhered to a sandwich of MgF_2/Ag/MgF_2 layers on a bottom Ag film. The top of the Ag layer can serve as a resonator, which can generate the SPR effect to help the impedance matching condition. The dielectric layer can form a resonance cavity and result in the CPR effect, which benefits the absorbance of the incident EM wave. The bottom Ag film acts as a mirror to prevent transmission and serves as a reflective layer to achieve maximum absorption and reduce reflection. Figure 1(b) shows the cross section of the unit cell and the geometrical parameters. The geometric parameters include the period (P), the width of the Ag nanobar (L), the gap between a pair of Ag nanobars (g), the thickness of a pair of Ag nanobars (d_1), the thickness of the first layer of MgF2 film (d_2), the thickness of the the the first layer of Ag film (d_3), the thickness of the the the second layer of the MgF_2 film (d_4), and the thickness of the the bottom layer of Ag film (d_5). We use COMSOL Multiphysics [39,

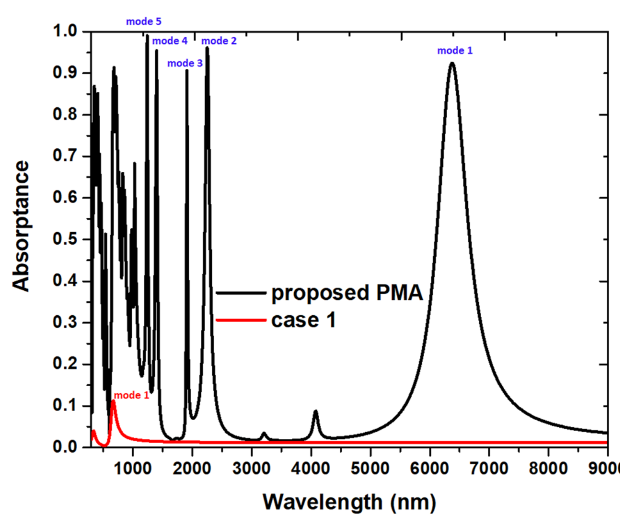

Fig. 2 Comparison of absorptance at resonance wavelength of the PMA without a pair of Ag nanobar (upper panel, case 1) and with a pair of Ag nanobar (bottom panel, proposed PMA), respectively. The structural parameters used for the FEM simulations are provided in Table 1

Table 2 Initial structural parameters of the proposed PMA

P (nm)	g (nm)	L (nm)	d_1 (nm)	d_2 (nm)	d_3 (nm)	d_4 (nm)	d_5 (nm)
2400	540	800	50	10	10	170	100

40], a commercially available FEM-based software, with a 2-D simulation model because the z-axis in Fig. 1 is infinite compared to the x and y-axes. The incident EM wave polarizes on the x-axis from the top plane of the proposed PMA, with normal incidence.

To mimic an infinite array of the unit cell system, periodic boundary conditions are considered in the x-direction, while perfectly matching layers are applied along the y-direction to absorb reflection waves at boundary interfaces. Ag permittivity of Ag is obtained from references [41, 42], and the RI of the MgF_2 layer is 1.37. Absorptance, which is the amount of incident radiation absorbed by the PMA, can be expressed as $A(\omega) = 1—R(\omega)—T(\omega)$, where $R(\omega) = |S_{11}(\omega)|^2$ and $T(\omega) = |S_{21}(\omega)|^2$ represent reflectance and transmittance, respectively. The full width at half maximum (FWHM) is defined as the bandwidth value between the left and right of the transmittance spectrum's half-maximum position. The dipping strength (ΔD) represents the variation between the maximum and minimum transmittance, calculated as $\Delta D = (T_{max} - T_{min}) \times 100\%$ [43]. Furthermore, the quality factor (QF) can be calculated as $QF = \lambda_{res}/FWHM$, where QF represents the sharpness of the resonance peak.

The proposed PMA's absorptance resonant peaks can be explained by the equivalent LC circuit model (shown in Fig. 1(c)) [15, 17, 44–46]. The model includes the capacitance between the nanobars in adjacent unit cells, which can be calculated as $C_{gap} = \varepsilon_0 d_1/(P–2L - g)$, where ε_0 is the permittivity of the permittivity of the surrounding medium's permittivity [45]. Additionally, the capacitance $C_m = c_1\varepsilon_2\varepsilon_0(2L + g)/d_2$ represents the capacitance between the nanobars and the Ag film. The coefficient c_1 accounts for the nonuniform charge distribution on the metal surface, and ε_2 is the permittivity of the dielectric layer. This model provides a clear understanding of the PMA's absorptance behavior.

The total impedance is [31].

$$Z_{tot} = \frac{i\omega(L_m + L_e)}{1 - \omega^2 C_{gap}(L_m + L_e)} - \frac{2i}{\omega C_m} + i\omega(L_m + L_e) \quad (1)$$

where the corresponding parameters are listed in Table 1.

The effect of the the second layer of MgF_2 film (d_4) and the bottom layer of the Ag film (d_5) can be ignored since C_{gap} is less than C_m [14, 15, 20, 31, 45]. Magnetic resonance occurs when the circuit has zero impedance. Therefore, the resonance condition of the PMA can be solved by setting Z_{tot} equal to zero. Then, the λ_{res} is [44]

$$\lambda_{res} \approx 2\pi\ \varepsilon_0\ ((L_m + L_e)C_m)^{1/2} \quad (2)$$

The design of the PMA configuration is suitable for fabrication using e-beam lithography, which has a resolution below 5 nm [47]. Furthermore, the grinding of the ion beam can also be used to make PMA, which is a common technique in nanotechnology [48–51]. Furthermore, spacer lithography is a promising technique for creating nanoshell arrays with uniform patterns and thicknesses of sub-10 nm [52, 53], making it compatible with the proposed design. Therefore, the designed PMA can be fabricated using existing nanofabrication techniques, which is essential for practical applications.

Inspection of the Structure Mechanism and the PMA Performance

Figure 2 illustrates a comparison between the absorptance spectra of the designed PMA in two cases: without (top panel, referred to as case 1 hereafter) and with (bottom panel, proposed PMA) a pair of Ag nanobars. FEM simulations used the structural parameters listed in Table 2.

The significant difference in the absorptance peaks between the two cases can be attributed to the hybridization of SPR, gap plasmon resonance (GPR), and CPR occurring in the proposed PMA. The absorptance spectrum and ΔD reveal that the case 1 only has one absorptance peak with low absorptance (17.23%) at $\lambda_{res} = 670$ nm. On the contrary, the proposed PMA exhibits quintuple-band absorptance with

Table 3 The λ_{res} (nm), FWHM (nm), A (%), Q factor, and ΔD of the cases 1 and proposed PMA structures corresponding to their resonance modes (i.e., at λ_{res})

	case 1	Proposed PMA				
mode	1	1	2	3	4	5
λ_{res} (nm)	670	1240	1400	1910	2250	6370
FWHM (nm)	120	20	18	20	90	600
A (%)	17.23	99.11	95.43	90.66	96.19	92.44
Q factor	5.58	62.00	77.78	95.50	25.00	10.62
ΔD (%)	11.11	98.98	95.41	90.64	96.17	92.42

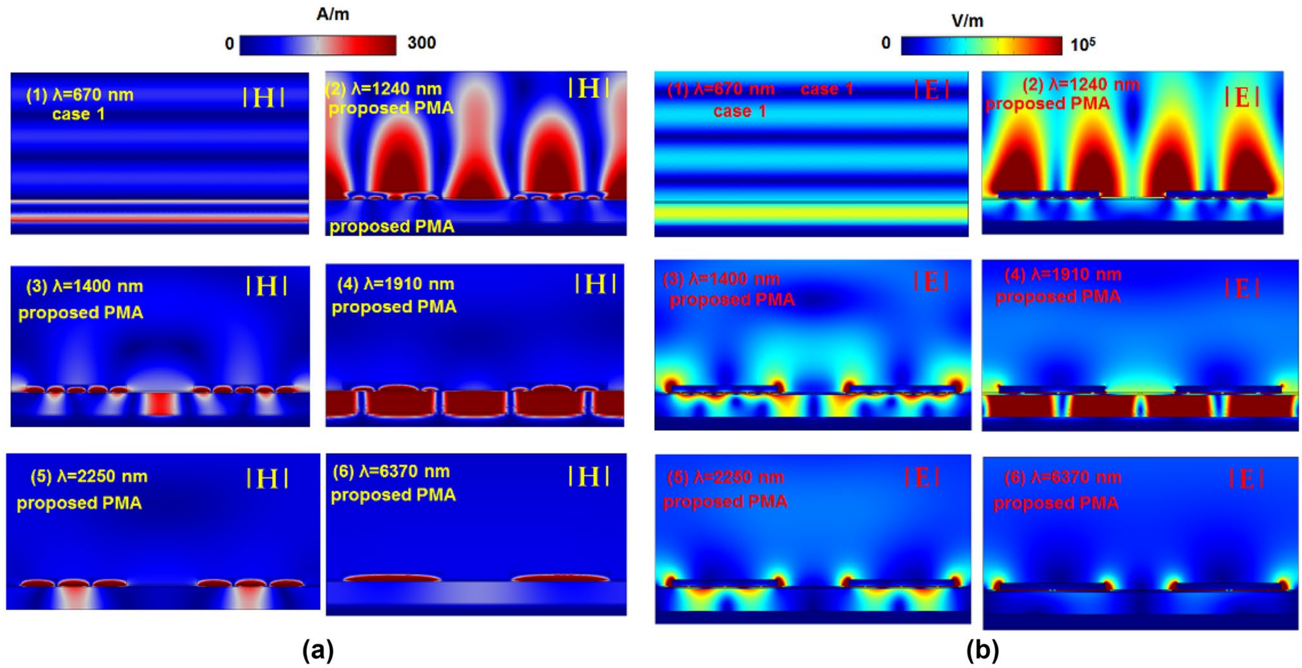

Fig. 3 **a** Magnetic field intensity distributions (|H|, A/m) and **b** electric field intensity (|E|, V/m) at resonance wavelength of the proposed PMA without a pair of Ag nanobars (case 1, see (1)) and with a pair of Ag nanobars (proposed PMA, see (2)–(6)), respectively

absorptance ranging from 90.66% to 99.11% at $\lambda_{res} = 1240$ nm, 1400 nm, 1910 nm, 2250 nm, and 6370 nm, corresponding to modes 1 to 5, respectively. The proposed PMA structure shows a remarkable improvement in absorptance peaks, Q-factor, ΔD, and small FWHM compared to the case 1. This improvement is due to the dielectric cavities formed by

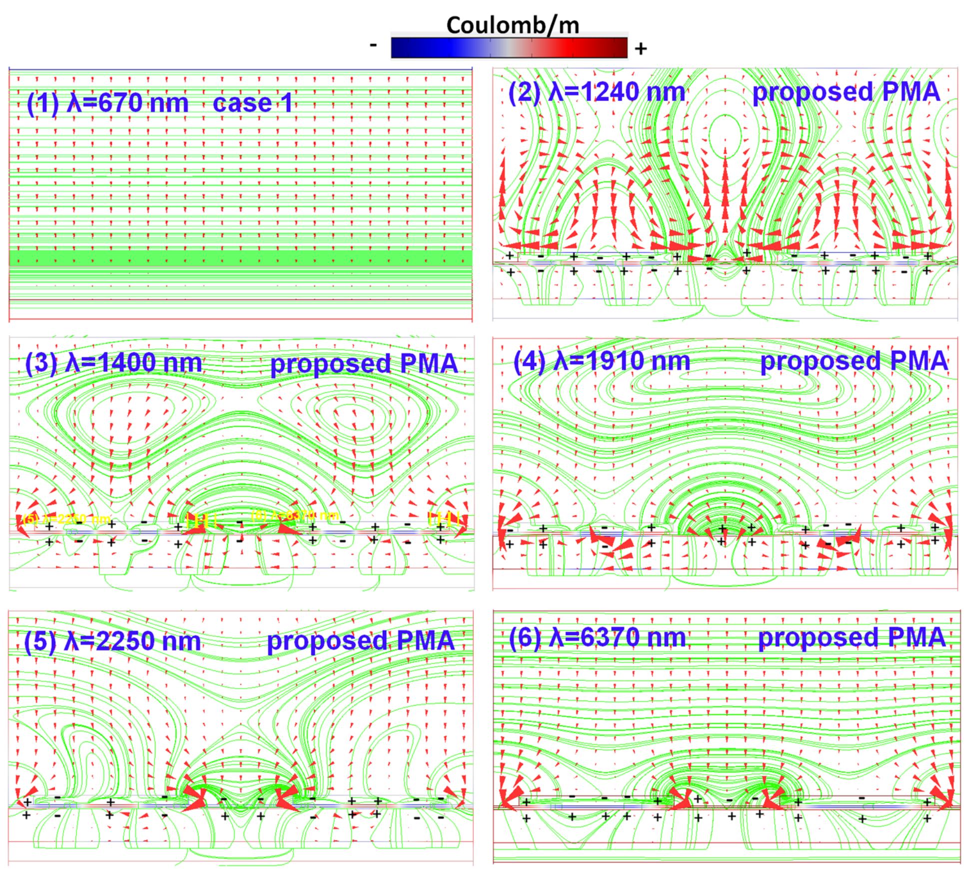

Fig. 4 Line charge density (Coulomb/m), electric force lines, and energy flow arrows of Case 1 (1) and the proposed PMA (2)–(6) in corresponding λ_{res}, respectively

MgF_2 between a pair of Ag nanobars and Ag layers, which can enhance the effects of CPR and GPR, and the top and edge surface of a pair of Ag nanorods that can provide an excellent light-matter intersection to enhance SPR [54, 55].

The remarkable improvement in absorptance in the proposed PMA structure results in SPPs in the unit cell center that provide quintuple-band near perfect absorptance and suppress intrinsic Ohmic losses in the plasmonic system [56]. By minimizing reflectance and eliminating transmittance, we achieved a nearly perfect absorber. Additionally, the redshifts observed in the proposed structure can be ascribed to the effective increase in capacitance and inductance of the resonant PMA, leading to an enhanced light-matter interaction. Table 3 summarizes the resonance wavelength (λ_{res} in nm), full width at half maximum (FWHM in nm), absorptance (A in %), Q factor and ΔD of the cases 1 and proposed PMA structures corresponding to their respective resonance modes (that is, at λ_{res}).

Figure 3(a), (b) provide a detailed visualization of the magnetic field intensity (|H|, A/m) and the electric field intensity (|E|, V/m) for Case 1 (Fig. 3(a)(1))) and the proposed PMA (Fig. 3(a)(2)–(6)) at λ_{res}. The four layers of Ag-nanobar/MgF_2/Ag/MgF_2 are designed to minimize reflection by matching the impedance at different material interfaces, while the bottom Ag layer acts as a mirror to prevent light transmission. It is evident that incident EM waves are efficiently confined to the respective metal surfaces, cavities, and edges at the corresponding λ_{res}. Compared to case 1, the fields ∣ H ∣ and ∣ E ∣ in the proposed PMA are much stronger and are concentrated in the gaps, edges, and top surfaces of a pair of Ag nanobars in the form of SPR and GPR, and in the MgF_2 layer in the form of CPR. The proposed PMA shows a notable in the confinement of plane enhancement in |H| and |E| in the gaps, dielectric cavities, and metal surfaces and a remarkable out-plane enhancement following the surface and edge enhancement adjacent to their external borders. Additionally, the pattern of ∣ H ∣ and ∣ E ∣ fields on metal surfaces, edges, and dielectric cavities is different from case 1 due to the presence of a pair of Ag nanobars in the proposed PMA, and the different λres. At shorter λ_{res} = 1240 nm, the enhanced SPR effect is obvious (Fig. 3(a)(2), (b)(2)), while at longer λ_{res}, a strong CPR effect is remarkable (Fig. 3(a)(4), (b)(4)). The gaps and cavities in the proposed PMA

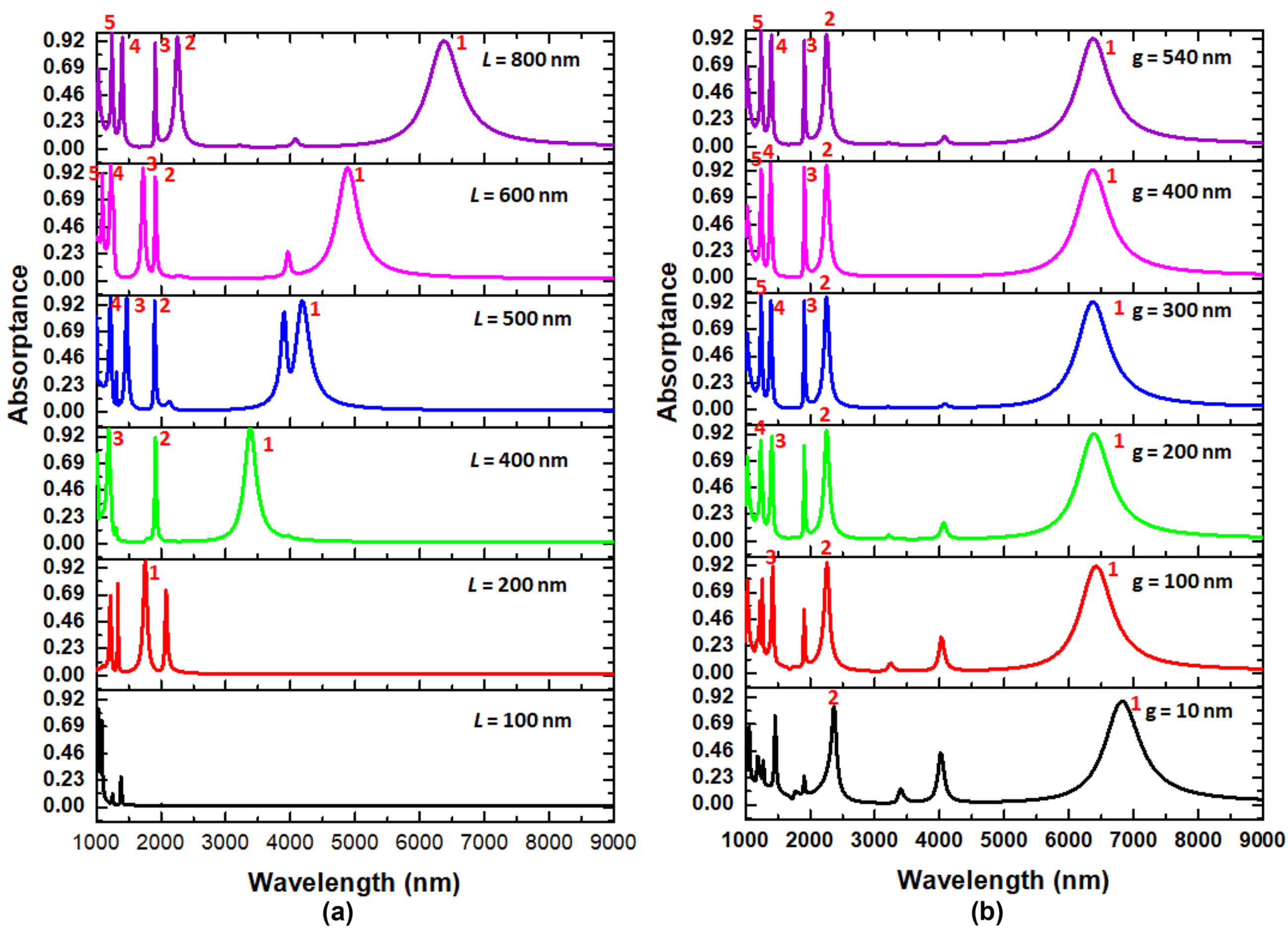

Fig. 5 Comparison of the absorptance spectrum of the proposed PMA by varying (**a**) *L* and (**b**) *g*, respectively

conduct the SPP sources and generate the GPR and CPR modes, while the surfaces of Ag nanobars and Ag layers contribute the SPR modes. Therefore, the proposed PMA significantly enhances the light-matter interaction and contributes to the quintuple-band absorptance peaks. Localized | H | and | E | fields induce an induced current loop, which can be understood by the magnetic polaritons and the LC circuit model [57].

Figure 4 illustrates the distribution of the enhanced electric field by mapping the distribution of positive and negative surface charge densities, electric force lines, and energy flow arrows. At the corresponding λ_{res}, the line charge density (Coulomb / m), the electric force lines (green lines), and the energy flow (red arrows) for cases 1 and the proposed PMA are shown. In cases 1 (Fig. 4(1)), the density of (+-) charge pairs is much weaker than in the proposed PMA, resulting in blurred charge pairs on the metal surface. In contrast, the proposed PMA (Fig. 4(1)–(6)) exhibits a more extensive distribution of charge pairs on the Ag surface between the second and last layers of MgF_2. The dipole-like charge pattern on the surface of the proposed PMA is controlled by hybridization of the SPR, GPR, and CPR modes, which is significant. The Ag surface between the second and last layers of MgF_2 is crucial in connecting the (+-) charge pairs in the plasmonic system, resulting in a stronger dipolar effect and increased mutual inductance on the metal surfaces, as well as capacitive coupling in resonant cavities.

The structural parameters have a great impact on the absorptance spectrum of the designed PMA. By varying the geometrical parameters, one can tune the absorptance peak wavelengths that range from near-infrared to mid-infrared, showing the tunability and feasibility of the designed PMA. The function of the bottom Ag layer is the mirror surface. Since $d_5 = 100$ nm, the transmittance channel will prevent near-infrared and mid-infrared. In the following simulations, we keep $d_5 = 100$ nm and vary one of the other structural parameters (i.e., L, g, d_1, d_2, d_3, and d_4) while keeping the other parameters intact. The default parameters are shown in Table 1.

First, we investigate the influence of L and g, on the absorptance spectrum, as shown in Fig. 5(a), (b), respectively. In Fig. 5(a), the varying L shows a great influence on the absorptance peaks. The absorptance peak of mode 1 redshifts with increasing L (from $\lambda_{res} = 1380$ nm to $\lambda_{res} = 6370$ nm), and the number of λ_{res} that absorptance exceeds 90% (labeled by

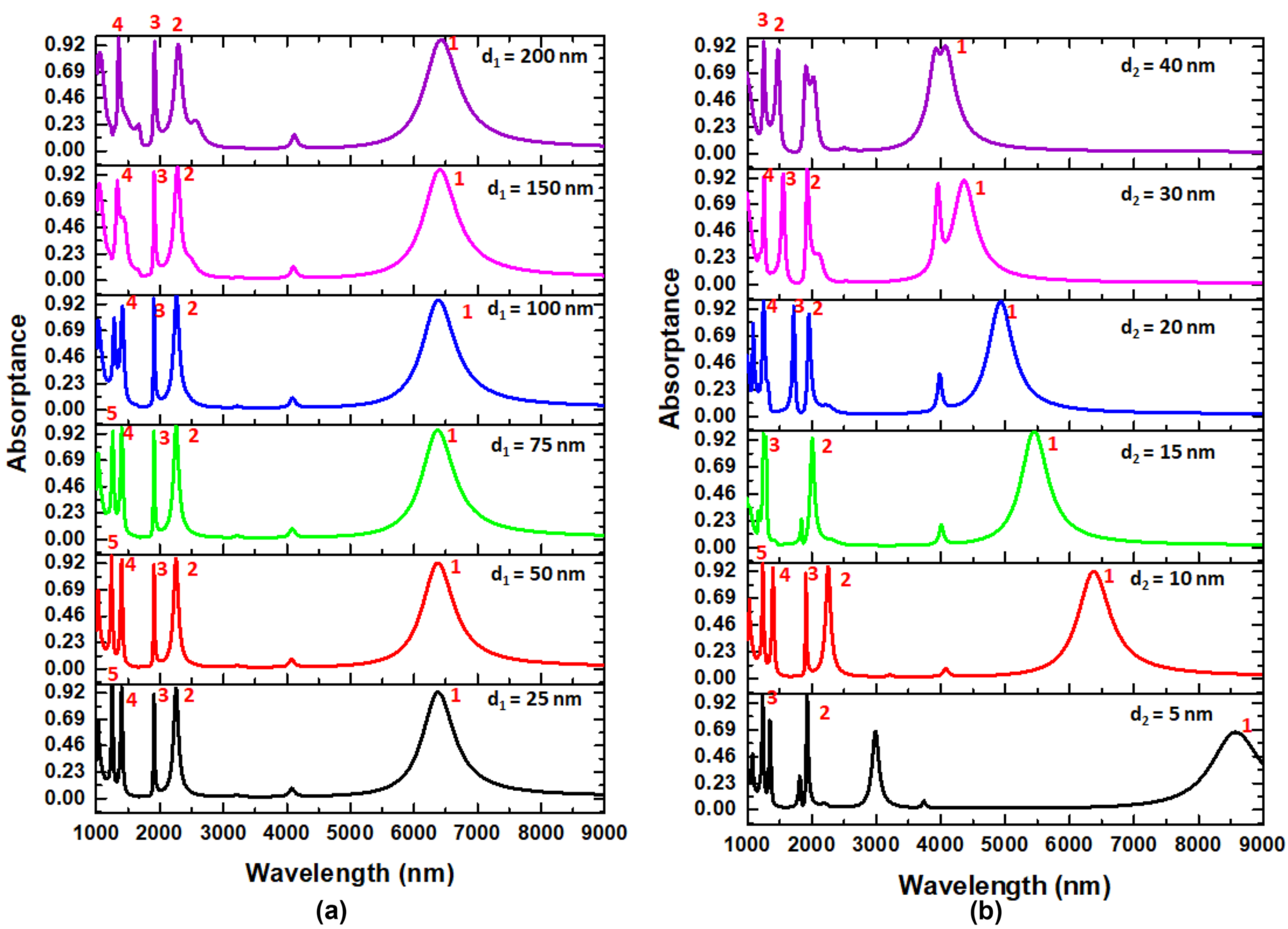

Fig. 6 Comparison of the absorptance spectrum of the proposed PMA by varying (**a**) d_1 and (**b**) d_2, respectively

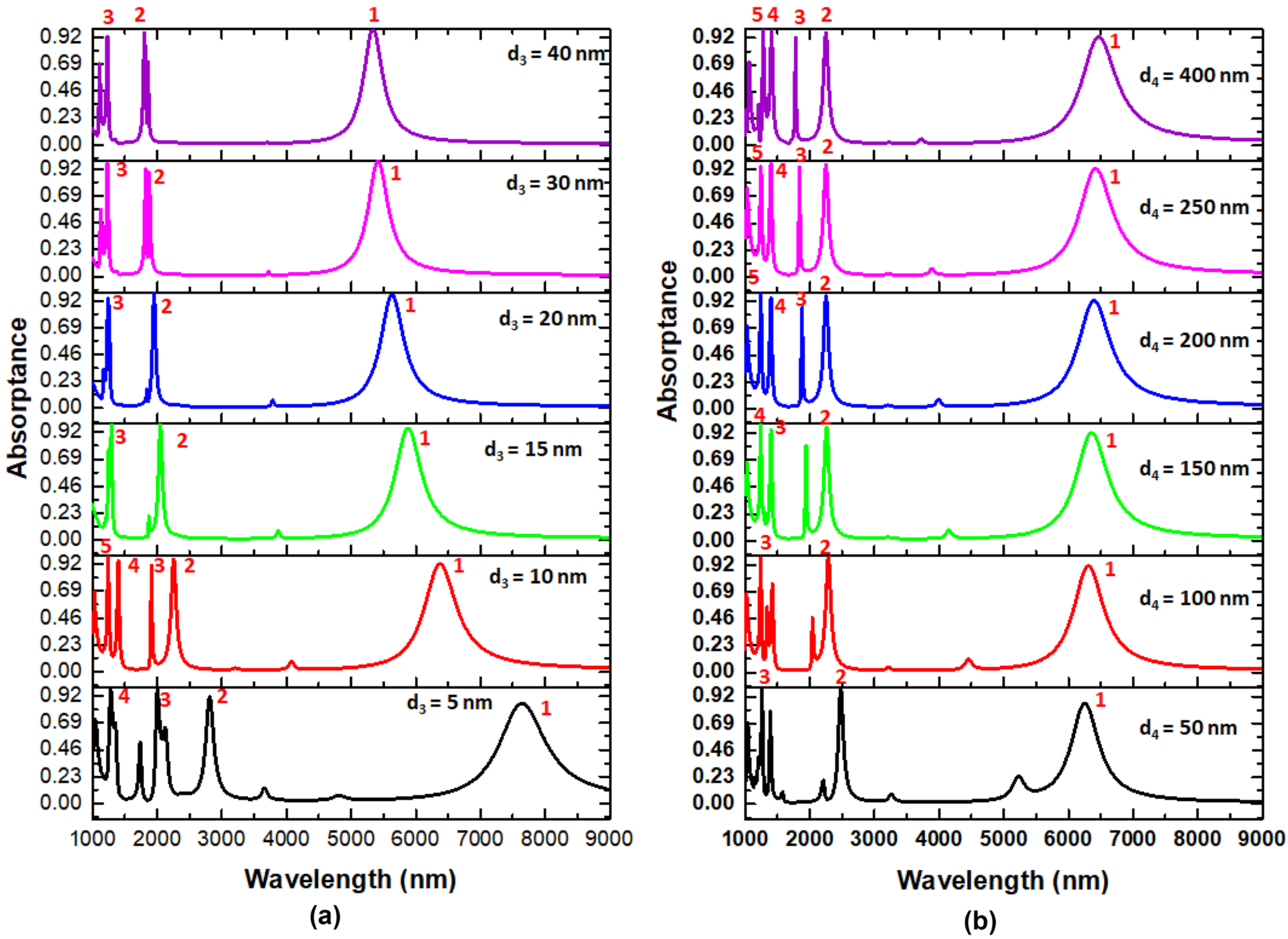

Fig. 7 Comparison of the absorptance spectrum of the proposed PMA by varying (**a**) d_3 and (**b**) d_4, respectively

number) increases with increasing L (from 0 to 5). This phenomenon can be described by the significant bound states of SPR on the top surface of longer Ag nanobars originating from the mechanics of the equivalent LC circuit. In the LC model (see Eq. (2) and Table 1), the λ_{res} increases with increasing L. In Fig. 5(b), the available ranges of g based on the desired working λ_{res} in the near and mid infrared regions and ΔD are 200 nm < g < 540 nm. Variation in g supports the coupling plasmon mode between a pair of Ag nanobars on the top surface.

The thickness of Ag nanobars (d_1), the first layer of MgF_2 (d_2), the thin layer of Ag (d_3) and the second layer of MgF_2 (d_4) can mediate the coupling effect of the SPP modes and significantly influence the performance of the absorptance spectrum. Figures 6(a), (b) and 7(a), (b) depict the absorptance spectrum of varying d_1, d_2, d_3, and d_4, respectively. As seen, the variations of d_2 (Fig. 6(b)) and d_3 (Fig. 7(a)) reveal a more significant blue shift with the increase of d_2 (from 8580 to 4070 nm) and d_4 (from 7640 to 5340 nm) when d_2 and d_4 increase from 5 to 40 nm. Note that there is a weak absorption peak at λ_{res} around 4000 nm. When the parameters of d_2 are changed, it will strongly couple with mode 1, resulting in a significantly enhanced plasmon mode. This is because an increase in d_2 forms an effective resonance cavity between the Ag nanobar and the Ag thin layer, leading to improved cavity plasmon resonance (CPR) and facilitating coupling with mode 1.

At the relevant wavelength, the skin depth of the Ag film measures approximately 11 nm. Figure 7(a) indicates that absorptance peaks shift towards the red with increasing thickness of the first layer of Ag, denoted as d_3. The thickness of the first layer of Ag (d_3) has a significant impact on resonance peaks. When d_3 exceeds 20 nm, there is almost no transmission power. The number of peaks remains at 3 for d_3 values greater than or equal to 15 nm. However, for d_3 values of 5 nm and 10 nm, the number of peaks is 4 and 5, respectively. The thickness of d_3 can influence the CPR effect between the Ag nanobar (with thickness d_1) and the Ag film (with thickness d_3) due to the different degrees of SPR effect resulting from varying d_3 thicknesses. According to Figs. 6 and 7, the available ranges of d_1, d_2, d_3, and d_4 based on the labeled numbers and desired λ_{res} in the near- and mid-infrared regions are

25 nm < d_1 < 200 nm, 5 nm < d_2 < 40 nm, 5 nm < d_3 < 40 nm, and 50 < d_4 < 400 nm, respectively, revealing reliability and tolerance in the fabrication of the proposed PMA structure, giving robust performance against fabrication imperfections. Therefore, the proposed PMA is favorable for practical application due to its outstanding robustness.

The LC model as seen in Eq. (2) and Table 1 shows that an increase in the width (L) and permittivity of the dielectric layer (ε_2) results in an increase in the λ_{res}. On the other hand, an increase in the thickness of the dielectric layer (d_2) leads to lower values of L_eC_m, while the term L_mC_m remains independent of d_2. Similarly, an increase in the thickness of the first layer of the dielectric (d_1) results in smaller values of L_eC_m, while the term L_mC_m remains unaffected by d_1. As a result, the λ_{res} decreases as the thickness of d_1 and d_2 increases. These predicted λ_{res} match well with the simulated results shown in Figs. 5, 6 and 7, which demonstrate the impact of d_2, L, and d_1. The thickness of the dielectric layer (d_1) solely influences the value of $C_g = \pi\varepsilon_0/(g/d_1)$, which is a weak factor. Therefore, the impact of g on the λ_{res} may be negligible, aligning with the simulated results shown in Fig. 5(b).

Conclusion

Using FEM simulation, we designed a periodic structure that comprises of a metallic nanobar array, a thin Ag film, and a dielectric layer. This quintuple band nearly perfect metamaterial absorber (PMA) operates in the near- and mid-infrared regions. We explored the influence of various structural parameters on the PMA's performance. The absorptance of the PMA we designed can reach 98.02%, 99.47%, 98.02%, 99.47%, and 96.09% for modes 1–5, respectively. Moreover, the PMA exhibits strong electric field confinement and enhancement in a nanogap region. The high absorptance is due to the hybridization of localized gap, cavity and surface plasmon resonance, which are influenced by the dielectric layer structure parameters. The proposed PMA significantly enhances the light-matter interaction and contributes to the quintuple-band absorptance peaks. The localized | H | and | E | fields induce an induced current loop, which can be explained by the magnetic polaritons and the LC circuit model. By adjusting the working wavelength, this design can be extended to other energy conversion applications. In conclusion, our study reveals that this PMA structure has multiple absorption channels and exhibits excellent performance.

Author Contributions Writing-original draft preparation and simulations were carried out by Chung-Ting Chou Chao. Methodology, formal validation analysis, and investigation were carried out by Sy-Hann Chen and Hung Ji Huang. The conceptualization, review, and editing was performed by Yuan-Fong Chou Chau.

Funding This work was supported by the University Research Grant from Universiti Brunei Darussalam (Grant No. UBD/RSCH/1.9/FICBF(b)/2022/018).

Data Availability The data that support the findings of this study are available from the corresponding author upon reasonable request.

Declarations

Ethics Approval There is no ethical approval required. Not applicable.

Consent to Participate Informed consent was obtained from all participants.

Consent to Publish Informed consent was obtained from all authors.

Conflicts of Interest The authors declare that they have no conflict of interest.

References

1. Sadrolhosseini AR, Ghasemi E, Pirkarimi A, Hamidi SM, Ghahrizjani RT (2023) Highly Sensitive Surface Plasmon Resonance Sensor for Detection of Methylene Blue and Methylene Orange Dyes Using Nico-Layered Double Hydroxide. Optic Commun 529: 129057
2. Mei C, Yuan Wu, Qiu S, Yuan J, Zhou X, Long K (2022) Design of Dual-Core Photonic Crystal Fiber for Temperature Sensor Based on Surface Plasmon Resonance Effect. Optic Commun 508:127838
3. Achanta VG (2020) Surface Waves at Metal-Dielectric Interfaces: Material Science Perspective. Rev Phys 5:100041
4. Ping R, Ma H, Cai Y (2019) Compact and Highly-Confined Spoof Surface Plasmon Polaritons with Fence-Shaped Grooves. Sci Rep 9(1):12045
5. ang W, Chou Chau YF, Jheng SC (2013) Analysis of Transmittance Properties of Surface Plasmon Modes on Periodic Solid/Outline Bowtie Nanoantenna Arrays. Phys Plasma 20(6):064503
6. Babicheva VE (2023) Optical Processes Behind Plasmonic Applications. Nanomaterials 13(7):1270
7. Mogilnaya TY, Krit BL, Morozova NV, Kuvshinov VV, Sleptsov VV, Vasiliev AM, Diteleva AO, Fedotikova MV, Pagava LL, Gorozheev MY (2021) The Effect of Nonmetallic Impurities on the Occurring of the Surface Plasmon Resonance at the Deposition of Nanocluster Coatings onto the Surface of Photo-Electric Converters. Optic Commun 494:127065
8. Dogan Y, Katirci R, Erdogan İ, Yartasi E (2023) Artificial Neural Network Based Optimization for Ag Grated D-Shaped Optical Fiber Surface Plasmon Resonance Refractive Index Sensor. Optic Commun 534:129332
9. Ou K, Wan H, Wang G, Zhu J, Dong S, He T, Yang H, Wei Z, Wang Z, Cheng X (2023) Advances in Meta-Optics and Metasurfaces: Fundamentals and Applications. Nanomaterials 13(7):1235
10. Ali A, Mitra A, Aïssa B (2022) Metamaterials and Metasurfaces: A Review from the Perspectives of Materials, Mech Adv Metadevices 12(6):1027
11. Liu J, Shan Wu, Ren Z, Jinyi Xu, Sheng Z (2023) Tunable Broadband Terahertz Properties in an Architecture Optimized Ito/Vo2 Hybrid Metamaterial. Optic Commun 537:129402
12. Zhang S, Qin M, Wu B, Wu E (2023) All-Dielectric Si Metamaterials with Electromagnetically Induced Transparency and Strong Gap-Mode Electric Field Enhancement. Optic Commun 530:129143
13. Landy NI, Sajuyigbe S, Mock JJ, Smith DR, Padilla WJ (2008) Perfect Metamaterial Absorber. Phys Rev Lett 100(20):207402

14. Wang H, Wang L (2015) Tailoring Thermal Radiative Properties with Film-Coupled Concave Grating Metamaterials. J Quant Spectrosc Radiat Transfer 158:127–135
15. Bai Y, Zhao Li, Dongquan Ju, Jiang Y, Liu L (2015) Wide-Angle, Polarization-Independent and Dual-Band Infrared Perfect Absorber Based on L-Shaped Metamaterial. Opt Express 23(7):8670–8680
16. Kumar N, Suthar B, Rostami A (2023) Novel Optical Behaviors of Metamaterial and Polymer-Based Ternary Photonic Crystal with Lossless and Lossy Features. Optic Commun 529:129073
17. Wang H, Wang L (2013) Perfect Selective Metamaterial Solar Absorbers. Optic Express 21(S6):A1078-A93
18. Cortés E, Wendisch FJ, Sortino L, Mancini A, Ezendam S, Saris S, de S. Menezes L, Tittl A, Ren H, Maier SA (2022) Optical Metasurfaces for Energy Conversion. Chem Rev 122(19):15082–176
19. So S, Mun J, Park J, Rho J (n/a) Revisiting the Design Strategies for Metasurfaces: Fundamental Physics, Optimization, and Beyond. Adv Mater n/a(n/a):2206399
20. El-Aasser M (2014) Design Optimization of Nanostrip Metamaterial Perfect Absorbers. J Nanophotonics 8(1):083085
21. Wang J, Chen Y, Hao J, Yan M, Qiu M (2011) Shape-Dependent Absorption Characteristics of Three-Layered Metamaterial Absorbers at near-Infrared. J Appl Phys 109(7):074510
22. Feng L, Huo P, Liang Y, Ting Xu (2020) Photonic Metamaterial Absorbers: Morphology Engineering and Interdisciplinary Applications. Adv Mater 32(27):1903787
23. Li Y, Li D, Chi C, Huang B (2017) Achieving Strong Field Enhancement and Light Absorption Simultaneously with Plasmonic Nanoantennas Exploiting Film-Coupled Triangular Nanodisks. J Phys Chem C 121
24. Tsai SR, Hamblin MR (2017) Biological Effects and Medical Applications of Infrared Radiation. J Photochem Photobiol B 170:197–207
25. Üstün K, Turhan-Sayan G (2017) Ultra-Broadband Long-Wavelength Infrared Metamaterial Absorber Based on a Double-Layer Metasurface Structure. J Opt Soc Am B 34:456
26. Wang Z, Chen J, Khan SA, Li F, Shen J, Duan Q, Liu X, Zhu J (2022) Plasmonic Metasurfaces for Medical Diagnosis Applications: A Review. Sensors 22(1):133
27. Singh AK, Mittal S, Das M, Saharia A, Tiwari M (2023) Optical Biosensors: A Decade in Review. Alexandria Eng J 67:673–91
28. Liu Y, Zhang X (2021) Microfluidics-Based Plasmonic Biosensing System Based on Patterned Plasmonic Nanostructure Arrays. Micromachines 12(7):826
29. Chau Y-F, Yeh H-H (2011) A Comparative Study of Solid-Silver and Silver-Shell Nanodimers on Surface Plasmon Resonances. J Nanopart Res 13(2):637–644
30. Han Y, Huang J-A, Liu X-Y, Zhang X-J, Shi J-X, Yan C-C (2016) Polarization-Independent Broadband Plasmonic Absorber Based on a Silicon-Nanowire Array Decorated by Gold Nanoparticles at the Optical Regime. Opt Express 24(9):9178–9186
31. Wu D, Liu Y, Li R, Chen L, Ma R, Liu C, Ye H (2016) Infrared Perfect Ultra-Narrow Band Absorber as Plasmonic Sensor. Nanoscale Res Lett 11(1):483
32. Cao C, Cheng Y (2018) Quad-Band Plasmonic Perfect Absorber for Visible Light with a Patchwork of Silicon Nanorod Resonators. Materials 11(10):1954
33. Cheng Y, Hui Luo Fu, Chen, Gong R (2019) Triple Narrow-Band Plasmonic Perfect Absorber for Refractive Index Sensing Applications of Optical Frequency. OSA Continuum 2(7):2113–2122
34. Luo S, Zhao J, Zuo D, Wang X (2016) Perfect Narrow Band Absorber for Sensing Applications. Opt Express 24(9):9288–9294
35. Feng R, Ding W, Liu L, Chen L, Qiu J, Chen G (2014) Dual-Band Infrared Perfect Absorber Based on Asymmetric T-Shaped Plasmonic Array. Optic Express 22(S2):A335-A43
36. Chen D, Bijun Xu, Xue X, Wang X, Hao Y (2023) Ultra-Broadband Dual-Square Ring Metamaterial Absorbers from Visible to Far-Infrared Region. Optic Commun 530:129124
37. Ma S, Zhang P, Mi X, Zhao H (2023) Highly Sensitive Terahertz Sensor Based on Graphene Metamaterial Absorber. Optic Commun 528:129021
38. Hao J, Wang J, Liu X, Padilla WJ, Zhou L, Qiu M (2010) High Performance Optical Absorber Based on a Plasmonic Metamaterial. Appl Phys Lett 96(25):251104
39. Chau YF, Tsai DP (2007) Three-Dimensional Analysis of Silver Nano-Particles Doping Effects on Super Resolution near-Field Structure. Opt Commun 269:389–94
40. Chen MW, Chau YF, Tsai DP (2008) Three-Dimensional Analysis of Scattering Field Interactions and Surface Plasmon Resonance in Coupled Silver Nanospheres. Plasmonics 3(4):157
41. Gharbi T, Barchiesi D, Kessentini S, Maalej R (2020) Fitting Optical Properties of Metals by Drude-Lorentz and Partial-Fraction Models in the [0.5;6] Ev Range. Opt Mat Express 10(5):1129–1162
42. Chau YF, Chao CT, Huang HJ, Wang YC, Chiang HP, Idris MN, Masri Z, Lim CM (2019) Strong and Tunable Plasmonic Field Coupling and Enhancement Generating from the Protruded Metal Nanorods and Dielectric Cores. Results Phys 13:102290
43. Yu J, Zhu J, Ye S, Wang X (2021) Ultra-Wide Sensing Range Plasmonic Refractive Index Sensor Based on a Two-Dimensional Circular-Hole Grating Engraved on a Gold Film. Results Phys 26:104396
44. Wu D, Li R, Liu Y, Zhongyuan Yu, Li Yu, Chen L, Liu C, Ma R, Ye H (2017) Ultra-Narrow Band Perfect Absorber and Its Application as Plasmonic Sensor in the Visible Region. Nanoscale Res Lett 12(1):427
45. Feng R, Qiu J, Liu L, Ding W, Chen L (2014) Parallel Lc Circuit Model for Multi-Band Absorption and Preliminary Design of Radiative Cooling. Optic Express 22(S7):A1713-A24
46. Wang LP, Zhang ZM (2011) Phonon-Mediated Magnetic Polaritons in the Infrared Region. Optics Express 19(S2):A126-A35
47. Ronchi A, Sterzi A, Gandolfi M, Belarouci A, Giannetti C, Del Fatti N, Banfi F, Ferrini G (2021) Discrimination of Nano-Objects Via Cluster Analysis Techniques Applied to Time-Resolved Thermo-Acoustic Microscopy. Ultrasonics 114:106403
48. Xu X, Yang Q, Wattanatorn N, Zhao C, Chiang N, Jonas SJ, Weiss PS (2017) Multiple-Patterning Nanosphere Lithography for Fabricating Periodic Three-Dimensional Hierarchical Nanostructures. ACS Nano 11(10):10384–10391
49. Park Y-B, Im M, Im H, Choi Y-K (2010) Superhydrophobic Cylindrical Nanoshell Array. Langmuir 26(11):7661–7664
50. Seol M-L, Im H, Moon D-I, Woo J-H, Kim D, Choi S-J, Choi Y-K (2013) Design Strategy for a Piezoelectric Nanogenerator with a Well-Ordered Nanoshell Array. ACS Nano 7(12):10773–10779
51. Choi Y-K, Zhu Ji, Grunes J, Bokor J, Somorjai GA (2003) Fabrication of Sub-10-Nm Silicon Nanowire Arrays by Size Reduction Lithography. J Phys Chem B 107(15):3340–3343
52. Chen Y, Shu Z, Zhang S, Zeng P, Liang H, Zheng M (2021) Sub-10 Nm Fabrication: Methods and Applications. Int J Extreme Manuf 3
53. De Angelis F, Malerba M, Patrini M, Miele E, Das G, Toma A, Zaccaria RP, Di Fabrizio E (2013) 3d Hollow Nanostructures as Building Blocks for Multifunctional Plasmonics. Nano Lett 13(8):3553–58.
54. Chau YF, Liu CY, Yeh HH, Tsai DP (2010) A Comparative Study of High Birefringence and Low Confinement Loss Photonic Crystal

Fiber Employing Elliptical Air Holes in Fiber Cladding with Tetragonal Lattice. J Progress In Electromagnetics Research B 22:39–52
55. Chau YF, Lin YJ, Tsai DP (2010) Enhanced Surface Plasmon Resonance Based on the Silver Nanoshells Connected by the Nanobars. Optic Express 18(4):3510–18
56. Chou Chao CT, Chou Chau YF, Chiang HP (2022) Biosensing on a Plasmonic Dual-Band Perfect Absorber Using Intersection Nanostructure. ACS Omega 7(1):1139–49
57. Lee BJ, Wang LP, Zhang ZM (2008) Coherent Thermal Emission by Excitation of Magnetic Polaritons between Periodic Strips and a Metallic Film. Opt Express 16(15):11328–11336